Aeroelastic stability of a flexible ribbon rotor blade

Jerome Sicard[a], Jayant Sirohi[b],[*]

[a] Google[X], 2175 Monarch St, Alameda, CA 94501, United States
[b] Department of Aerospace Engineering and Engineering Mechanics, The University of Texas at Austin, Austin, TX 78712, United States

ARTICLE INFO

Keywords:
Ribbon rotor
Aeroelastic stability
Flexible blade
Classical flutter
Divergence

ABSTRACT

This paper describes the static and dynamic aeroelastic behavior of a thin ribbon that is used as an extremely flexible helicopter rotor blade. The non-dimensional torsional stiffness of this rotor blade is three orders of magnitude lower than that of a conventional helicopter rotor blade. As a result, the rotor blade undergoes large torsional deformation and its static and dynamic behavior are dominated by centrifugal forces. An aeroelastic analysis is developed based on Euler–Bernoulli beam theory including large twist angles and unsteady aerodynamics including the effect of returning wake. The flow is assumed to be attached at all times, and only classical divergence and flutter stability are evaluated. The analysis is validated with deformation measurements of a 23 cm diameter rotor with ribbon blades. Divergence and flutter stability boundaries are identified, and the effects of rotational speed, rotor diameter, location of blade center of gravity and blade pitch are discussed. The analysis can be used as a design tool for flexible ribbon rotors in a variety of missions.

1. Introduction

Conventional helicopter rotor blades are typically long, slender structures constructed out of stiff materials such as metals or composites, with a closed-cell cross-section. This paper describes the aeroelastic behavior of an unconventional rotor blade comprised of a thin ribbon with a mass at the tip. The cross-section of the ribbon is a circular arc, and the ribbon is constructed out of a low shear modulus carbon fiber layup. This ribbon rotor blade has negligible structural stiffness. Its dynamic behavior is dominated by centrifugal and aerodynamic forces, and hence it is prone to aeroelastic instability.

In the 1960's, ribbon rotor blades were explored for heavy lift helicopters with large diameter rotors. These early flexible rotor blades consisted of a thin membrane (e.g. mylar, fabric or metal) supported by cables running spanwise and stabilized by a tip mass (Winston, 1968b, 1968a; Roeseler, 1966; Goldman, 1960; Linden, 1972). Simplified analyses of such blades indicated that stability boundaries were independent of rotational speed (Roeseler, 1966; Goldman, 1960) and limited experiments were performed to quantify their dynamic response. In addition, these analyses showed that divergence stability was assured when the elastic axis was ahead of the aerodynamic center, and flutter was prevented when the blade center of gravity was ahead of the elastic axis. These conclusions contrast with the classical criterion for aeroelastic stability of a conventional rigid rotor blade (Johnson, 2013), which only requires the blade to be mass balanced in such a way that the center of gravity is ahead of the aerodynamic center, and where the location of the elastic axis is of relatively minor importance.

Recently, Sicard and Sirohi (2014b) investigated extremely flexible, ribbon blades for a 46 cm diameter micro-helicopter rotor. These blades consisted of a thin flexible matrix composite ribbon, with a circular arc cross-section that served as the airfoil profile. A cylindrical tip body oriented chordwise at an index angle to the blade provided centrifugal stiffening and created a passive twist

---

(a) Flexible ribbon rotor at rest.   (b) Flexible ribbon rotor at 1500 RPM.

(c) Planform of ribbon rotor blade.
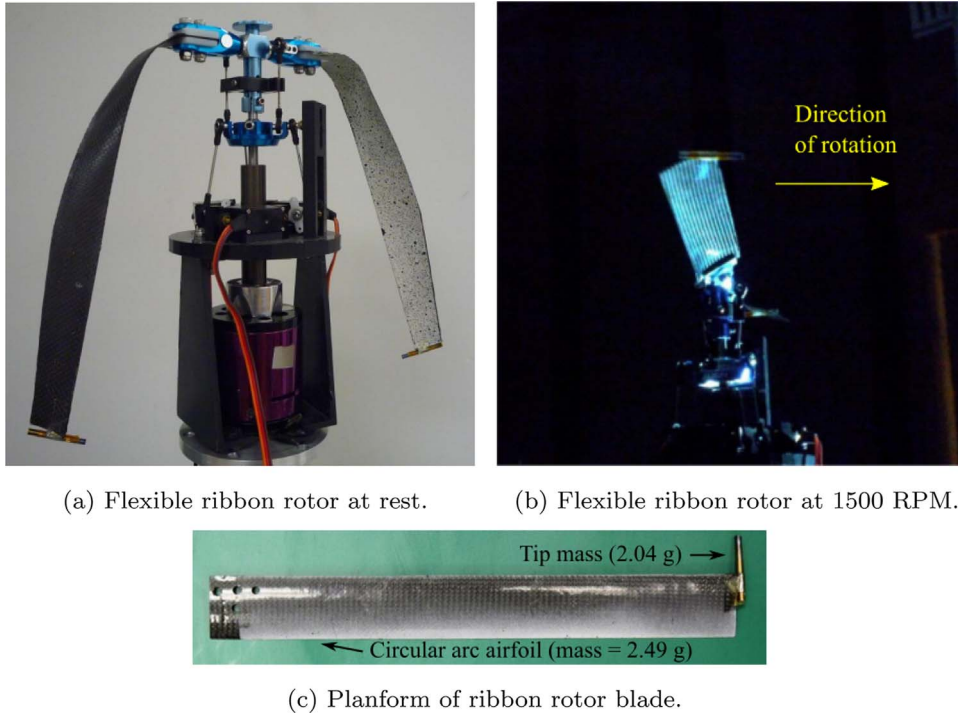
Fig. 1. Experiments on 46 cm diameter flexible ribbon rotor.

Table 1
Ribbon rotor parameters.

Airfoil		Circular arc
Rotor radius	R	22.86 cm
Ribbon blade length	L	17 cm
Chord	c	2.286 cm
Camber	C_a	7.5% of c
Thickness	t	1.39% of c
Total blade mass	M_B	4.53 g
Tip mass	M_m	2.04 g
Tip mass index angle	θ_{ind}	−22°
Rotational speed	Ω	1200 rpm
Tip Reynolds number	Re_c	46,160

Table 2
Ribbon rotor blade material properties and normalized stiffnesses.

Young's modulus	E	25 GPa
Shear modulus	G	1 MPa
Flap bending stiffness	$\dfrac{EI_\eta}{m_0\Omega^2R^4}$	9.65×10^{-2}
Lead-lag bending stiffness	$\dfrac{EI_\xi}{m_0\Omega^2R^4}$	2.54×10^1
Torsional stiffness	$\dfrac{GJ}{m_0\Omega^2R^4}$	1.00×10^{-3}

distribution. Fig. 1(a) shows a picture of the flexible ribbon rotor at rest with the rotor blades hanging under their own weight. A picture of the rotor spinning at 1200 rpm (Fig. 1(b)) taken under stroboscopic illumination shows the rotor blade stiffened by centrifugal force, and the blade planform is shown in Fig. 1(c). The parameters of this rotor are listed in Table 1 and the material properties of the ribbon are listed in Table 2. Note that the non-dimensional torsional stiffness of this ribbon rotor blade is three orders of magnitude lower than that of a conventional rotor blade.

Experiments in hover showed that these blades could generate the same thrust and efficiency as rigid rotor blades with the same planform. However, in contrast to previous analytical predictions, the stability boundaries of these rotor blades was found to depend on rotational speed and collective pitch (blade root pitch angle). Therefore, guided by these experiments, a more refined aeroelastic

analyses was developed by the authors to capture the dynamic response of flexible ribbon rotor blades and to predict the stability boundary. This paper describes the aeroelastic analysis, its experimental validation, and discusses some key results.

2. Aeroelastic analysis

An aeroelastic analysis was developed to explore the stability boundaries of this flexible ribbon rotor blade in hover. The structural model of the blade is based on one-dimensional beam theory and the aerodynamic model is two-dimensional strip theory including unsteady effects. The present study only investigates classical aeroelastic instabilities, i.e., divergence and flutter that are based on small perturbations for which the flow can be assumed attached at all times. This assumption considerably simplifies the analysis. Because of the negligible structural stiffness of the rotor blade, centrifugal stiffening plays a key role. Of particular interest is the torsional dynamics of the rotor blade, specifically the effect of centrifugal force on a thin ribbon undergoing large twist deformation. The resulting restoring moment, or equivalently, the axial foreshortening due to twisting of the ribbon, is called the trapeze effect and has a significant effect on the structural response. The trapeze effect on a thin ribbon is discussed in detail by Sicard and Sirohi (2014a).

First, the equations of motion are derived using the extended Hamilton's principle:

$$\int_{t_1}^{t_2} [(\delta T - \delta U - \delta V_g + \delta W_a)_b + (\delta T - \delta V_g)_m] \mathrm{d}t = 0 \tag{1}$$

where δT, δU and δV are the variations of kinetic, strain and potential energies respectively. The subscripts $()_b$ and $()_m$ indicate energies of the blade airfoil and the tip mass respectively, and δW_a accounts for the virtual work done by aerodynamic forces. Solution of the time invariant terms in Eq. (1), along with quasi-steady aerodynamic forces, results in the steady-state equilibrium deformation of the rotor blade. The equations of motion are then linearized to obtain a system of equations for small perturbations $\Delta \mathbf{q}$ about the equilibrium position.

$$(\mathbf{M} - \mathbf{M^a})\Delta \ddot{\mathbf{q}} + (\mathbf{G} - \mathbf{C^a})\Delta \dot{\mathbf{q}} + (\mathbf{K} - \mathbf{K^a})\Delta \mathbf{q} = \mathbf{0} \tag{2}$$

where $\mathbf{M}$, $\mathbf{G}$, $\mathbf{C}$ and $\mathbf{K}$ are the mass, gyroscopic, damping and stiffness matrices respectively, and the superscript 'a' refers to aerodynamic terms. The equations of motion are discretized using the finite element method, with each element consisting of 14 degrees of freedom (3 axial displacements, 4 bending displacements, 4 bending slopes and 3 twist angles) distributed over three nodes. Divergence and flutter instabilities are identified using the $p - k$ method (Hodges and Pierce, 2002), using an efficient numerical scheme proposed by Hassig (1971). Details of the structural and aerodynamic models of the rotor blade are given below.

2.1. Blade coordinate system and displacement variables

The rotor blade is modeled as an Euler–Bernoulli beam, where each cross-section undergoes three elastic displacements u, v and w, representing the extensional, lead-lag bending (in the rotor plane $x - y$) and flap bending (normal to the rotor plane) deflections of points located on the elastic axis (Fig. 2). Each cross-section can also undergo a rotation $\bar{\theta}$ about the deformed elastic axis. It can be shown that, for small strains, this rotation can be expressed in terms of the pitch angle at the root of the rotor blade θ_0, the elastic twist deformation ϕ and the bending deflections as

$$\bar{\theta} = \theta_0 + \phi - \int_0^x \frac{w'}{\sqrt{1 - v'^2 - w'^2}} \left(v'' + \frac{v'w'w''}{1 - w'^2} \right) d\chi \tag{3}$$

where the primes denote a spatial derivative with respect to x. Note that the sectional angle of incidence, i.e., the pitch angle, that determines the aerodynamic loads is $\theta = \bar{\theta} - \theta_0$.
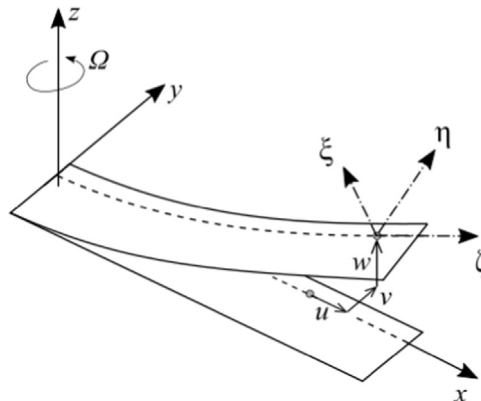

Fig. 2. Blade rotating at a constant angular velocity Ω with coordinate systems and deflections.

Table 3
Ordering scheme.

$\theta_0,\ \theta,\ \phi,\ \dfrac{x}{R},\ \dfrac{\partial}{\partial x},\ \dfrac{\partial}{\partial t} = \boldsymbol{O}(1)$
$\dfrac{v}{R},\ \dfrac{w}{R},\ \dfrac{\eta}{R},\ \dfrac{\xi}{R},\ \dfrac{c}{R} = \boldsymbol{O}(\epsilon)$
$\dfrac{u}{R} = \boldsymbol{O}(\epsilon^2)$

2.2. Ordering and truncation scheme

To simplify the equations of motion, the terms in Eq. (1) are first ordered by their relative magnitudes and then truncated to retain second-order accuracy. When combining kinetic and potential energies in the Hamiltonian, the relative magnitude of inertial terms with respect to structural terms must be considered and an appropriate ordering scheme must be chosen such that all physically significant terms are retained. A consistent truncation scheme retains the self-adjoint property of the structural and inertial operators, i.e., the mass and stiffness matrices must remain symmetric and the gyroscopic matrix must remain anti-symmetric after the truncation.

Along the lines of previous studies (Hodges and Dowell, 1974; Kaza and Kvaternik, 1977; Bir et al., 1990), an ordering scheme is defined where each physical quantity is compared to a small parameter $\epsilon < 1$ that is on the order of the normalized flap bending deflection w/R. The ordering scheme is summarized in Table 3. Note that the present scheme specifically includes arbitrarily large pitch angles θ of order $\boldsymbol{O}(1)$, to capture the large twist deformation observed in experiments.

Two types of truncation strategies can be found in the literature. One strategy identifies an order of magnitude of terms to retain in the kinetic and potential energies (Hodges and Dowell, 1974; Bir et al., 1990) and subsequently makes some exceptions to include terms specific to physical phenomena of interest, such as blade warping and the trapeze effect. In the other strategy, the extensional, bending and torsional equations of motion are truncated to different orders (Kaza and Kvaternik, 1977), which can lead to loss of the self-adjoint property of the operators. A rigorous truncation strategy is employed in the present study: all strain energy terms of order greater than $\boldsymbol{O}(\epsilon^5)$ and all kinetic energy terms of order greater than $\boldsymbol{O}(\epsilon^3)$ are eliminated. This strategy automatically retains all terms associated with the torsional dynamics, i.e., the trapeze effect (strain energy $\boldsymbol{O}(\epsilon^4)$, kinetic energy $\boldsymbol{O}(\epsilon^3)$) and the propeller moment (no strain energy, kinetic energy $\boldsymbol{O}(\epsilon^2)$).

2.3. Structural model

The structural model yields the rotor blade strain energy, kinetic energy, and gravitational energy based on the assumed blade deformations (Section 2.1). Models of the nonlinear deformation of nonuniform rotating beams undergoing combined flap bending, lead-lag bending, torsion and extension have been developed by several researchers based on energy truncation schemes (Hodges and Dowell, 1974; Kaza and Kvaternik, 1977; Rosen and Friedmann, 1978) and geometrically exact theories (Hodges, 1985, 2006). The present study is based on an energy truncation scheme specifically tailored towards flexible rotor blades with large pitch angles, as described in Section 2.2.

Based on the ordering scheme, the sectional pitch angle can be written as

$$\theta = \phi - \int_0^x v'' w'\, d\chi + \boldsymbol{O}(\epsilon^4) \sim \phi - \int_0^x v'' w'\, d\chi \tag{4}$$

The total axial displacement can be written as a sum of the elongation u_e and the kinematic displacement, or foreshortening, due to bending and the trapeze effect (detailed derivation by Sicard and Sirohi (2014a)) as

$$u = u_e - \frac{1}{2} \int_0^x (v'^2 + w'^2 + k_A^2 \theta')\, d\chi \tag{5}$$

The variation in the strain energy is

$$\delta U = \int_R \iint_A (E\epsilon_{xx}\delta\epsilon_{xx} + 4G\epsilon_{x\eta}\delta\epsilon_{x\eta} + 4G\epsilon_{x\xi}\delta\epsilon_{x\xi})\, d\eta\, d\xi\, dx \tag{6}$$

The variation in the strain energy, with some key terms highlighted, is shown in Appendix A. The expression for variation in the strain energy can be linearized by first-order Taylor expansion about the equilibrium (or trim) position and written as

$$(\delta U)_{b\ Lin} = (\delta U)_{b\ 0} + \boldsymbol{\delta q}^T\, \mathbf{K}\, \boldsymbol{\Delta q} \tag{7}$$

where $\mathbf{K}$ is the contribution of the blade strain energy to the linearized stiffness matrix of the system.

The variation in the blade kinetic energy is given by

$$\delta T = \int_R \iint_A \rho\, \frac{d\mathbf{r_1}}{dt} \cdot \delta\left(\frac{d\mathbf{r_1}}{dt}\right) d\eta\, d\xi\, dx \tag{8}$$

where $\mathbf{r_1}$ is the position vector of a particle on the deformed blade. The variation in this position vector and the variation in kinetic

energy are shown in Appendix A. The variation in kinetic energy can be linearized about the equilibrium position as

$$(\delta T)_{b\,Lin} = (\delta T)_{b\,0} + \delta\mathbf{q}^T\,\mathbf{K}\,\Delta\mathbf{q} + \delta\mathbf{q}^T\,\mathbf{G}\,\Delta\dot{\mathbf{q}} + \delta\mathbf{q}^T\,\mathbf{M}\,\Delta\ddot{\mathbf{q}} \tag{9}$$

This $\mathbf{K}$ matrix is added to the stiffness matrix obtained from the strain energy, and $\mathbf{G}$ and $\mathbf{M}$ are the gyroscopic matrix and the mass matrix respectively.

Finally, the variation in the blade gravitational potential energy is

$$(\delta V_g)_b = g\int_R m_0\delta w - \{m_0 w'(d_\eta\sin\overline{\theta} + d_\xi\cos\overline{\theta})\}\delta w' + \left\{m_0\left(1 - \frac{w'^2}{2}\right)(d_\eta\cos\overline{\theta} - d_\xi\sin\overline{\theta})\right\}\delta\theta \tag{10}$$

where d_η and d_ξ are the offsets of the blade sectional center of gravity from the elastic axis, along and perpendicular to the blade sectional chord, respectively. The tip mass also contributes to the total kinetic energy and gravitational energy; these can be derived by following a similar procedure as described above and are given in Appendix A. The work done by aerodynamic forces on the tip mass is ignored.

2.4. Aerodynamic model

The virtual work done by aerodynamic forces and moments is calculated from 2-D strip theory assuming incompressible flow. Assuming that the blade airfoil of chord c experiences harmonic pitching $\alpha(t)$ and heaving $h(t)$ motion, and that the flow remains attached, the unsteady aerodynamic forces (lift per unit length L and pitching moment per unit length M) can be written as

$$L = C'\left\{\frac{1}{2}\rho U^2 c C_{lo} + \frac{1}{2}\rho U c C_{l\alpha}\left[(\dot{h} + U\alpha) + \left(x_A + \frac{c}{2}\right)\dot{\alpha}\right]\right\} + \frac{1}{2}\rho C_{l\alpha}\frac{c^2}{4}\left[(\ddot{h} + U\dot{\alpha}) + \left(x_A + \frac{c}{4}\right)\ddot{\alpha}\right] \tag{11}$$

$$M = C'\left\{\frac{1}{2}\rho U^2 c^2 C_{mo} - \frac{1}{2}\rho U^2 c C_{lo} x_A - \frac{1}{2}\rho U c C_{l\alpha} x_A\left[(\dot{h} + U\alpha) + \left(x_A + \frac{c}{2}\right)\dot{\alpha}\right]\right\}$$
$$+ \frac{1}{2}\rho C_{l\alpha}\frac{c^2}{4}\left[-\left(x_A + \frac{c}{4}\right)(\ddot{h} + U\dot{\alpha}) - \frac{c}{4}U\dot{\alpha} - \frac{c^2}{4}\left(\frac{3}{8} + \frac{2x_A}{c}\left(1 + \frac{2x_A}{c}\right)\right)\ddot{\alpha}\right] \tag{12}$$

where C' is the Theodorsen lift deficiency function including Loewy's correction to model the unsteady effect of the returning wake shed by blades in previous revolutions (Johnson, 2013), U is the resultant blade velocity and x_A is the distance of the aerodynamic center aft of the elastic center (see Fig. 3). The reduced frequency (k) for the unsteady aerodynamics is calculated at the 75% rotor radius. A profile drag force per unit length D is also included in the model, based on a constant profile drag coefficient C_{do}. The lift coefficients ($C_{l\alpha}$, C_{lo}) and pitching moment coefficient (C_{mo}) are obtained from a lookup table, which was calculated using ANSYS Fluent for the circular arc airfoil at a representative Reynolds number (at 75% rotor radius). Fig. 3 shows a schematic of the aerodynamic forces acting on the airfoil section. Note that the effective lift and pitching moment act at the aerodynamic center (AC) and include circulatory as well as non-circulatory components. The origin of the airfoil-fixed coordinate system (ξ–η) is at the elastic center (EC) of the section; the heaving and pitching motion of the airfoil is defined with respect to this point. The steady inflow of the rotor is calculated from classical blade element-momentum theory (BEMT).

The angle of attack is given in terms of the tangential (in the rotor plane) and normal components of incident velocity, U_T and $U_P = -(\dot{h} + U\alpha)$ respectively. In terms of the blade deformations, these can be written as

$$U_T = (\Omega x + \dot{v})\cos\overline{\theta} + (\dot{w} + V_i)\sin\overline{\theta} + \Omega v v'\cos\overline{\theta} + \Omega v w'\sin\overline{\theta} + \Omega u\cos\overline{\theta} - \Omega x\frac{v'^2}{2}\cos\overline{\theta} + O(\epsilon^3) \tag{13}$$

$$U_P = (\dot{w} + V_i)\cos\overline{\theta} - (\Omega x + \dot{v})\sin\overline{\theta} - \Omega v v'\sin\overline{\theta} + \Omega v w'\cos\overline{\theta} - \Omega u\sin\overline{\theta} + \Omega x\frac{v'^2}{2}\sin\overline{\theta} + O(\epsilon^3) \tag{14}$$

Also, the rate of change of angle of attack can be expressed to second order as

$$\dot{\alpha} = \dot{\theta} + \dot{v}'w' + \Omega w' \tag{15}$$

Finally, the virtual work done by the aerodynamic loads is

$$(\delta W_a)_b = \int_R (a_v\delta v + a_w\delta w + a_\theta\delta\theta)dx + O(\epsilon^5) \tag{16}$$
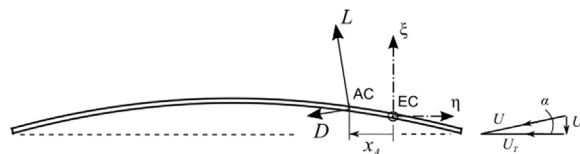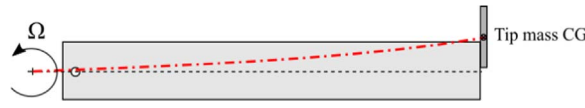

Fig. 3. Aerodynamic forces on 2D-section.

Fig. 4. Elastic axis determined by locus of the centroids of the radial stress field along the blade span.

where the generalized forces a_v and a_w, and the generalized moment a_θ are listed in Appendix B. After linearization, these terms contribute to the global mass, stiffness and damping matrices.

2.5. Sectional properties

The aerodynamic forces are transformed to the aerodynamic center (AC in Fig. 3), assumed to be located at the quarter-chord of the airfoil, which is justified for attached flow. The center of gravity of the blade is determined by the chordwise location of the tip mass, however, the center of gravity of each blade section is located at mid-chord because of the constant blade chord and thickness. The location of the elastic center (EC) is very important for the structural model. For conventional rotor blades, the elastic axis is the blade feathering axis, which is coincident with the pitch bearings. Typically, the elastic axis, which is the locus of the elastic centers, is located along the quarter-chord of the blade. For a thin ribbon (symmetric about mid-chord), the elastic axis is coincident with the mid-chord line. However, it can be shown that for thin ribbons under the influence of centrifugal force, i.e. for flexible blades undergoing large elastic twist, the elastic axis is the locus of the centroids of the radial stress field at each spanwise location (Sicard and Sirohi, 2014a). The shape of this elastic axis is illustrated in Fig. 4. Note that the position and shape of this axis changes as the blade deforms, however for simplicity, the present study calculates the elastic axis based on an undeformed geometry (ribbon with no bending or twist deformation) and assumes it does not change.

3. Results and discussion

First, the torsional dynamics of the rotor blade with tip mass is described. Then, the analysis is used to calculate the divergence and flutter boundaries of the blade at various collective pitch angles. Finally, the effect of a change in chordwise position of the tip mass, or in the rotor blade length on the stability boundaries is investigated.

3.1. Flexible blade dynamics

The analysis was used to calculate the rotating frequencies and mode shapes of the flexible blade. Fig. 5 shows a fan plot of the first five rotating natural frequencies of the flexible blade at 5° and 15° collective pitch. The dashed lines indicate multiples of rotor harmonics (denoted as /rev), which make it convenient to interpret the natural frequencies in terms of the nominal rotor speed (1200 rpm).

The mode shapes are labeled "*F*" for flap bending, "*L*" for lead-lag bending and "*T*" for torsion, to indicate the participation of the degree of freedom. This can be identified visually by plotting the mode shapes as in Fig. 6. It can be seen that:
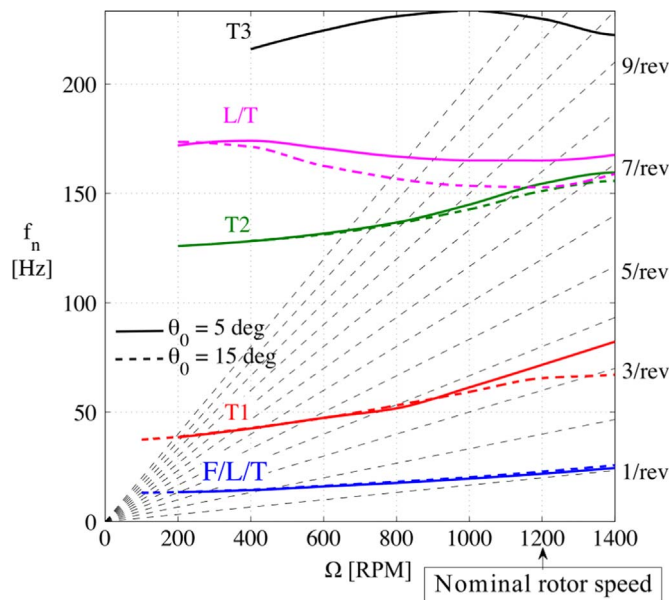

Fig. 5. Rotating natural frequencies of flexible rotor blade at 5° and 15° collective.
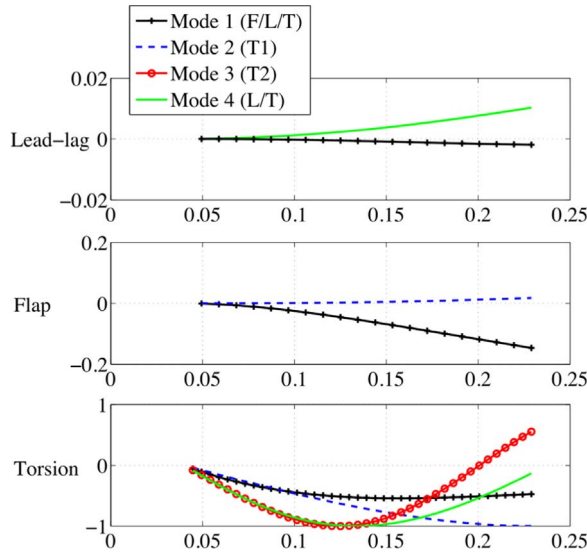
Fig. 6. Flexible blade rotating mode shapes ($\theta_0 = 0°$, Ω=1000 rpm).

(a) The first eigenmode (F/L/T) fully couples the flap, lag and pitch deformations.
(b) The second eigenmode (T1) and third eigenmode (T2) are predominantly torsional modes.
(c) The fourth mode (L/T) involves lag-torsion coupling. This mode is the most sensitive to the collective pitch, with the increased collective resulting in a decrease in frequency.
(d) The fifth mode (T3) (not shown in Fig. 6) is also predominantly a torsional mode.

A closer look at the lowest predominantly torsional mode (T1) of the flexible blade indicates the nature of the torsional dynamics. Fig. 7 plots the rotating torsional frequency of the flexible blade in vacuum as a function of blade material shear modulus. As the shear modulus decreases, i.e., the blade structural stiffness decreases, the importance of centrifugal stiffening becomes apparent. The rotating torsional frequency ν_θ of the flexible blade is on the order of 3.3/rev. As the shear modulus of the material approaches zero, it can be seen that the torsional frequency tends to 2/rev.

3.2. Validation with experiments

The aeroelastic analysis was validated with experimental measurements of the bending and twist deformation of a ribbon rotor blade in hover. The experimental setup and procedure are described in detail by Sicard and Sirohi (2013). Fig. 8 shows the experimentally measured blade pitch as a function of span for a ribbon rotor blade at 1200 rpm, at different collective pitch (θ_0) angles. Also shown for comparison are the numerical predictions from the aeroelastic model. Very good agreement can be seen over
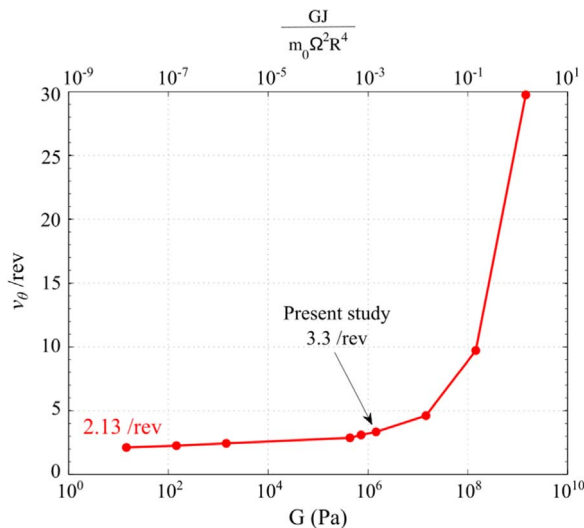

Fig. 7. Torsional natural frequency (in vacuum) of the flexible rotor blade as a function of blade shear modulus, at 1200 rpm and 15° collective pitch.
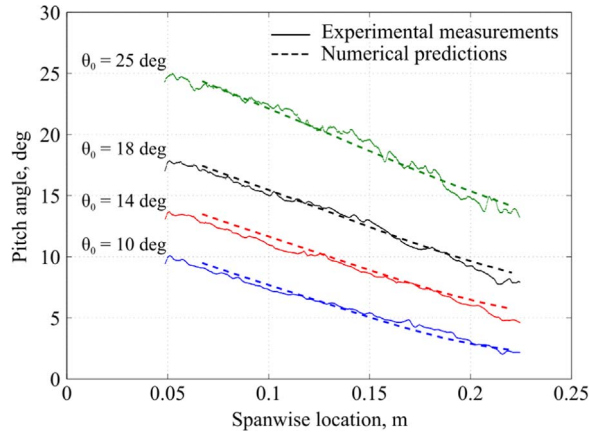
Fig. 8. Comparison of experimentally measured blade pitch with numerical predictions.

the span at all the collective pitch angles. The effect of different assumptions in the aeroelastic analysis was also explored, and it was found that neglecting the higher order twist terms resulted in a 50% error in the prediction of blade tip pitch angle. The validated aeroelastic analysis was then used to investigate the divergence and flutter boundaries of the ribbon rotor blade.

3.3. Divergence boundary of the ribbon rotor blade

Divergence occurs when the equilibrium position calculated by the trim analysis is statically unstable, i.e., if the determinant of the effective stiffness matrix becomes negative.

$$|\mathbf{K} - \mathbf{K}_a| < 0 \tag{17}$$

In conventional rotor blades, the divergence boundary depends on the chordwise position of the center of gravity with respect to the aerodynamic center. Therefore, the sign of the determinant in Eq. (17) was computed for various chordwise positions of the tip mass. First, the divergence stability was evaluated for the configuration experimentally tested in previous work (Sicard and Sirohi, 2012) (tip mass CG ahead of the AC by 34% chord). Then, the center of gravity of the tip mass was moved aft until divergence occurred. This procedure was repeated at four different rotational speeds (1200, 1500, 2000 and 3000 rpm) and the results are shown in Fig. 9. It can be seen that the torsional frequency of the rotor blade depends upon the position of the tip mass, as well as the rotational speed.

Moreover, Fig. 9 indicates that the blade is free from divergence when the center of gravity of the tip mass is located $0.34c$ ahead of the aerodynamic center, as in the experimental study. When the center of gravity of the tip mass is moved close to or aft of the aerodynamic center, the divergence boundary depends upon the rotational speed. For example, taking the case where the tip mass center of gravity is located at the aerodynamic center, we can see that the rotor blade is free from divergence at 1200 and 1500 rpm and becomes unstable at 2000 rpm. These results qualitatively agree with experimental observations of the rotor blade stability boundaries (Sicard and Sirohi, 2012).
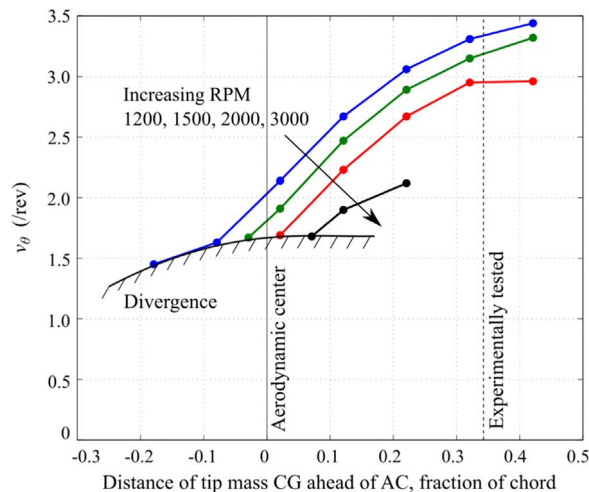

Fig. 9. Divergence stability boundary of ribbon rotor blade as a function of location of the tip mass and rotational speed.
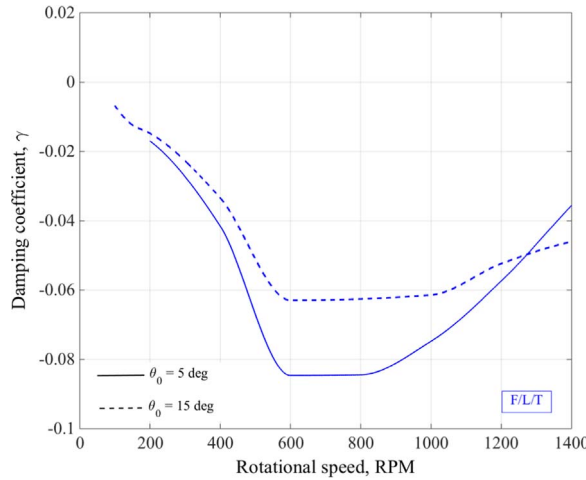
Fig. 10. Damping coefficient of flap-lag-torsion mode.

3.4. Flutter boundary of the ribbon rotor blade

Typically, the coalescence of two eigenmodes indicates the possibility of classical flutter. The fan plot in Fig. 5 shows coalescence between the eigenmodes $T2$ and L/T, for blade rotational speeds greater than 1100 rpm and for a collective pitch of 5°. The stable or unstable nature of a particular eigenmode can be determined by examining the real part of its eigenvalue p, which is related to the damping coefficient γ of that eigenmode by

$$\gamma = \frac{\Re(p)}{k} \tag{18}$$

A change in the sign of γ, from negative to positive, indicates the onset of flutter. The damping coefficients are plotted for the lowest eigenmode and the coalescing modes as a function of the rotational speed in Figs. 10 and 11.

Fig. 10 shows that the $F/L/T$ mode is unconditionally stable over the range of rotational speeds simulated (0–1400 rpm). The torsional modes (T1, T2 and T3) show similar behavior. However, the L/T mode becomes unstable at a rotational speed of Ω=1100 rpm (see Fig. 11). In this case, the onset of flutter is due to a coalescence between the L/T mode and the $T2$ mode, leading to unstable oscillations at approximately 8/rev. An important conclusion from this analysis is that the stability boundary is a function of the rotational speed. This result correlates with experimental observations of the blade in hover. It can also be seen (Fig. 11(a)) that at Ω=1250 rpm, the blade is predicted to be stable when $\theta_0 = 15°$ and unstable when $\theta_0 = 5°$. This result also agrees with previous experiments (Sicard and Sirohi, 2012), in which the blades were unstable at collective pitch lower than 10° when spinning at 1200 rpm.
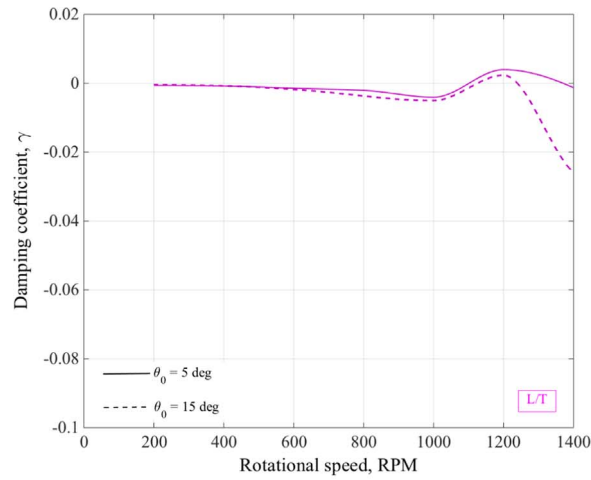
3.5. Influence of the chordwise position of the tip mass

The aeroelastic analysis can be used to investigate ways of enhancing the flutter stability of the flexible ribbon rotor blades. One of the design parameters is the chordwise position of the tip mass. As discussed in Section 3.3, this parameter has a significant effect on the divergence boundary. The analysis is now used to investigate the effect of moving the tip mass aft on the natural frequencies, damping ratio and mode shapes of the ribbon rotor blade.

Fig. 12 shows that the change in position of the tip mass predominantly affects the first two torsional modes of the rotor blade (modes $T1$ and $T2$). However, a decrease of the frequencies is observed, which is due to the change in the location of the elastic axis that results from the change in center of gravity of the tip mass. Nevertheless, by decreasing the frequencies associated with the third mode ($T2$) while keeping those of the fourth mode (L/T) relatively constant, coalescence of these two modes is avoided. Moreover, because the damping coefficients remain negative at all rotational speeds (Fig. 13), it can be inferred that moving the tip mass aft eliminates classical flutter and enables stable operation over a larger range of rotational speeds. Note that this result is counterintuitive; in a conventional rotor blade a decrease in stability margin is expected when the blade center of gravity is moved aft.

3.6. Effect of a change in rotor diameter

The analysis is also used to investigate the effect of a change in rotor blade length on the stability boundaries, for example, if the ribbon rotor blade changes its diameter in flight. In such a case, the rotor must still produce the same thrust and so, the rotational speed is adjusted such that the product $\Omega^2 R^3$ remains constant. For example, if a rotor is initially spinning at 1200 rpm and its diameter is doubled, it must spin at 425 rpm to create the same thrust. Fig. 14(a) shows the natural frequencies of the extended rotor blade at 15° collective pitch and for rotational speeds up to 300 rpm. Note that due to the slower rotational speeds, the magnitudes of

(a) Lag-torsion mode
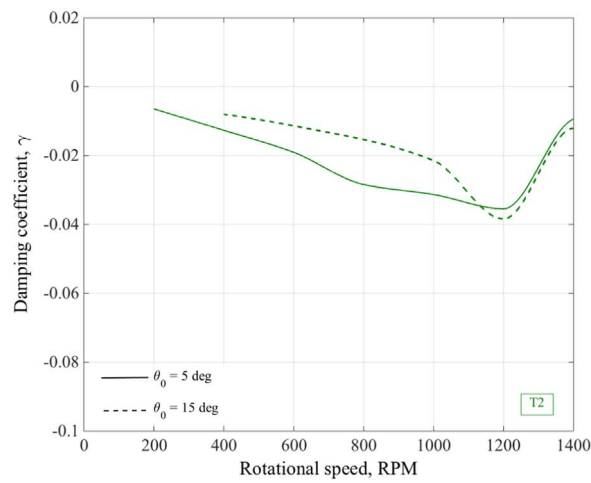
(b) Torsion mode 2

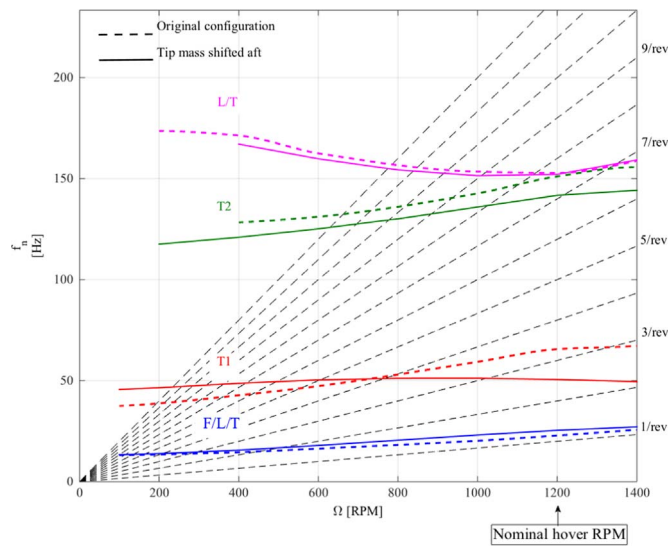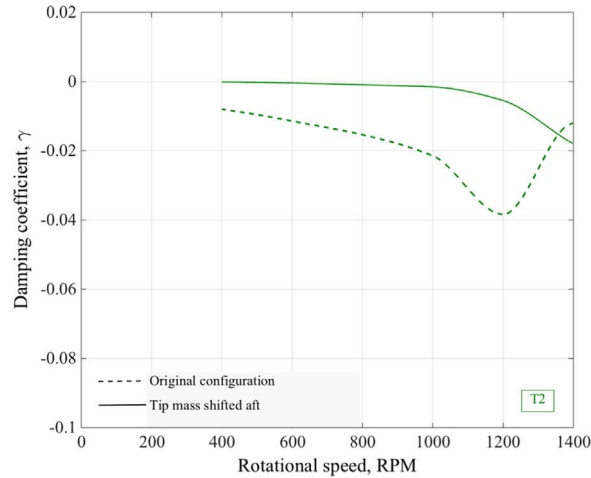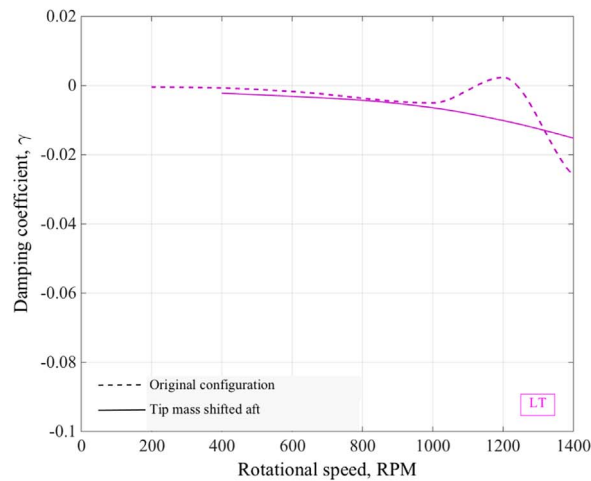**Fig. 11.** Damping coefficient of coupled lag-torsion and second torsional mode.

Fig. 12. Influence of the tip mass chordwise position on the natural frequencies.

(a) Torsion mode 2

(b) Lag-torsion mode

Fig. 13. Influence of the tip mass chordwise position on the damping of the second torsional mode and the coupled lag-torsion mode.

the natural frequencies of the deployed rotor are well under those corresponding to the original rotor. For clarity, only the frequencies of the extended rotor blade are shown. It can be seen that the change in rotor diameter affects predominantly the first torsional mode ($T1$) whose natural frequency increases and becomes closer to that of the second torsional mode ($T2$). Coalescence of the modes $T2$ and L/T is avoided, however the damping coefficient of the $T2$ mode becomes positive, resulting in an instability at around 220 rpm (Fig. 14(b)).

Overall, the change in rotor diameter leads to shifts in the natural frequencies and results in new stability boundaries. Therefore, for a variable-diameter ribbon rotor, the stability boundaries must be investigated for every rotational speed or rotor diameter that is possible during operation.

4. Summary and conclusions

The aeroelastic behavior of a flexible helicopter rotor blade was described. The ribbon rotor blade is comprised of a thin flexible matrix composite strip with a circular arc airfoil section and a cylindrical tip mass. Ribbon rotor blades have potential applications in heavy lift helicopters, variable-diameter morphing rotors and damage tolerant rotors. The non-dimensional torsional stiffness of this rotor blade is three orders of magnitude lower than that of a conventional helicopter blade. As a result, the ribbon rotor blade undergoes large twist deformation, and torsional as well as bending dynamics are dominated by centrifugal forces. In addition, such a rotor blade with negligible structural stiffness is prone to aeroelastic instabilities.

A numerical aeroelastic analysis of the ribbon rotor blade was developed specifically including the effects of large twist deformation. The analysis was validated with experimental measurements of deformation of a ∼23 cm radius ribbon rotor. The validated aeroelastic analysis was then used to predict the divergence and flutter boundary of the rotor blades in hover, and investigate the effect of design and control parameters on the stability margins. The analysis was based on the nonlinear coupled
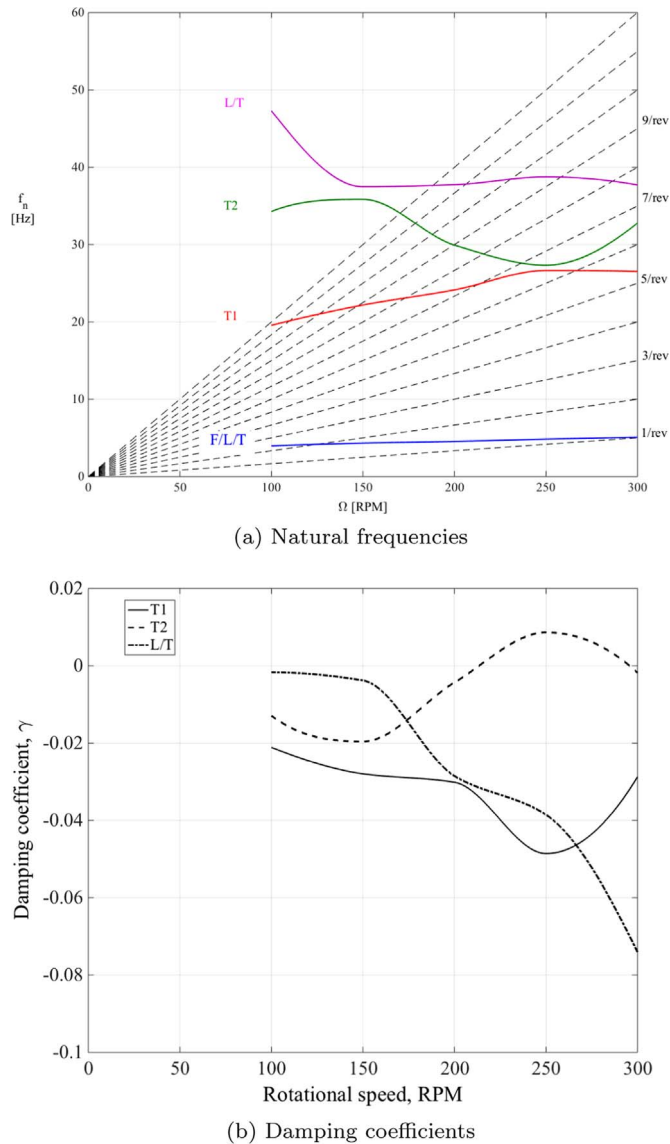
(a) Natural frequencies

(b) Damping coefficients

Fig. 14. Influence of the rotor diameter on the stability boundaries.

equations of motion of rotor blades with extension, lag, flap and torsion degrees of freedom. The blades were modeled as second-order isotropic Euler–Bernoulli beams experiencing small bending deflections but large twist angles. The aerodynamic model included unsteady effects based on Theodorsen's theory and equations were discretized and solved following a finite element approach. Onset of classical flutter instability was determined by the $p - k$ method, considering a typical section at the 75% radius location. The flutter analysis was conducted for various collective pitch angles and over a range of rotational speeds.

Classical flutter was observed to occur at the coalescence between the second torsional mode and the first coupled lag/torsion mode of oscillation of the rotor blade. It was found that changing the blade root pitch or the rotational speed affected the stability boundary, which agrees with experimental observations. In addition, it was shown that by moving the chordwise position of the tip mass center of gravity aft, the torsional frequencies of the new blade were uncoupled from the lag/torsion mode and flutter instability was avoided. However, the divergence stability margin was also reduced. In contrast, for conventional rotor blades, moving the blade center of gravity aft has a destabilizing effect.

Finally, the effect of a change in rotor diameter on the stability boundaries was investigated. Analytical predictions of frequencies and damping coefficients showed that a change in rotor diameter leads to shifts of the natural frequencies and therefore new stability boundaries. The results depend on the specific rotor parameters being kept constant during the change in diameter, for example, total rotor thrust. This result indicates that when designing a variable-diameter flexible ribbon rotor, the stability boundaries must be investigated for every operating rotor diameter. Note that this study only considered classical divergence and flutter; a complete stability analysis would require solution of the equations of motion in the time domain to investigate the presence of other

instabilities or limit cycle oscillations.

Appendix A. Variations of strain energy, kinetic energy and gravitational potential energy

A.1. Blade strain energy

From the blade strains, the variation in the strain energy can be derived as

$$(\delta U)_b = \int_R \left(s_{u'} \delta u' + s_{v'} \delta v' + s_{v''} \delta v'' + s_{w'} \delta w' + s_{w''} \delta w'' + s_\theta \delta\theta + s_{\theta'} \delta\theta' \right) dx + \boldsymbol{O}(\epsilon^6) \tag{A.1}$$

where

$$s_{u'} = EA\left(u' + \frac{v'^2}{2} + \frac{w'^2}{2}\right) + EA\frac{k_A^2}{2}\theta'^2 - (EAv'' + GA\theta'w')(e_\eta \cos\bar\theta - e_\xi \sin\bar\theta)$$

$$- (EAw'' - GA\theta'v')(e_\eta \sin\bar\theta + e_\xi \cos\bar\theta) \tag{A.2}$$

$$s_{v'} = EA\left(u' + \frac{v'^2}{2} + \frac{w'^2}{2}\right)v' + EA\frac{k_A^2}{2}v'\theta'^2$$

$$- (EAv'v'' + 2GAv'w'\theta')(e_\eta \cos\bar\theta - e_\xi \sin\bar\theta)$$

$$- \left(EAv'w'' - GAu'\theta' - \frac{3}{2}GAv'^2\theta'\right)(e_\eta \sin\bar\theta + e_\xi \cos\bar\theta) \tag{A.3}$$

$$s_{v''} = \left[EI_\xi \cos^2\bar\theta + EI_\eta \sin^2\bar\theta - EI_{\eta\xi}\sin 2\bar\theta\right]v''$$

$$+ \frac{1}{2}\left[(EI_\xi - EI_\eta)\sin 2\bar\theta + 2EI_{\eta\xi}\cos 2\bar\theta\right]w''$$

$$- \frac{EB_2}{2}\theta'^2 \cos\bar\theta + \frac{EB_3}{2}\theta'^2 \sin\bar\theta - EA(u' + \frac{v'^2}{2} + \frac{w'^2}{2})(e_\eta \cos\bar\theta - e_\xi \sin\bar\theta)$$

$$+ GJ\theta'w' \tag{A.4}$$

$$s_{w'} = EA\left(u' + \frac{v'^2}{2} + \frac{w'^2}{2}\right)w' + EA\frac{k_A^2}{2}w'\theta'^2$$

$$- (EAw'v'' + GAu'\theta' + GAv'^2\theta' + \frac{3}{2}GAw'^2\theta')(e_\eta \cos\bar\theta - e_\xi \sin\bar\theta)$$

$$- EAw'w''(e_\eta \sin\bar\theta + e_\xi \cos\bar\theta) + GJv''\theta' \tag{A.5}$$

$$s_{w''} = \left[EI_\xi \sin^2\bar\theta + EI_\eta \cos^2\bar\theta + EI_{\eta\xi}\sin 2\bar\theta\right]w''$$

$$+ \frac{1}{2}\left[(EI_\xi - EI_\eta)\sin 2\bar\theta + 2EI_{\eta\xi}\cos 2\bar\theta\right]v''$$

$$- \frac{EB_2}{2}\theta'^2 \sin\bar\theta - \frac{EB_3}{2}\theta'^2 \cos\bar\theta$$

$$- EA\left(u' + \frac{v'^2}{2} + \frac{w'^2}{2}\right)(e_\eta \sin\bar\theta + e_\xi \cos\bar\theta) \tag{A.6}$$

$$s_\theta = \frac{1}{2}\left[(EI_\xi - EI_\eta)\sin 2\bar\theta + 2EI_{\eta\xi}\cos 2\bar\theta\right]w''^2$$

$$-\frac{1}{2}\left[(EI_\xi - EI_\eta)\sin 2\bar\theta + 2EI_{\eta\xi}\cos 2\bar\theta\right]v''^2$$

$$+\left[(EI_\xi - EI_\eta)\cos 2\bar\theta - 2EI_{\eta\xi}\sin 2\bar\theta\right]v''w''$$

$$-\left(\frac{EB_2}{2}\cos\bar\theta - \frac{EB_3}{2}\sin\bar\theta\right)w''\theta'^2 + \left(\frac{EB_2}{2}\sin\bar\theta + \frac{EB_3}{2}\cos\bar\theta\right)v''\theta'^2$$

$$+\left[EA\left(u' + \frac{v'^2}{2} + \frac{w'^2}{2}\right)v'' + GAu'w'\theta' + GAv'^2w'\theta'\right.$$

$$\left. + GA\frac{w'^3\theta'}{2}\right](e_\eta\sin\bar\theta + e_\xi\cos\bar\theta)$$

$$+\left[-EA\left(u' + \frac{v'^2}{2} + \frac{w'^2}{2}\right)w'' + GAu'v'\theta'\right.$$

$$\left. + GA\frac{v'^3\theta'}{2}\right](e_\eta\cos\bar\theta - e_\xi\sin\bar\theta) \tag{A.7}$$

$$s_{\theta'} = EAk_A^2\left(u' + \frac{v'^2}{2} + \frac{w'^2}{2}\right)\theta' + \left(\frac{EB_1}{2}\right)\theta'^3 - (EB_2\sin\bar\theta + EB_3\cos\bar\theta)w''\theta'$$

$$-(EB_2\cos\bar\theta - EB_3\sin\bar\theta)v''\theta' + GJ\theta' + GJv''w'$$

$$-\left(GAu'w' + GAv'^2w' + \frac{GAw'^3}{2}\right)(e_\eta\cos\bar\theta - e_\xi\sin\bar\theta)$$

$$+\left(GAu'v' + \frac{GAv'^3}{2}\right)(e_\eta\sin\bar\theta + e_\xi\cos\bar\theta) \tag{A.8}$$

The terms with a double underline correspond to the extension-torsion coupling due to the trapeze effect. The terms with a single underline are related to bending–torsion coupling; these terms vanish for rotor blades with small angles of twist, and hence, they do not appear in conventional rotor blade studies (Hodges and Dowell, 1974; Kaza and Kvaternik, 1977; Bir et al., 1990). The terms with a dashed underline must be kept for arbitrary non-symmetric cross-sections. Finally, the wavy underlined terms are retained due to the consistent ordering scheme; these terms are arbitrarily neglected in other rotor blade analyses (Hodges and Dowell, 1974; Bir et al., 1990). The cross-sectional constants are defined in Appendix C.

A.2. Blade kinetic energy

The variation in kinetic energy can be derived and integrated by parts with respect to time to yield

$$\int_{t_1}^{t_2}(\delta T)_b = \int_{t_1}^{t_2}\int_R (k_u\delta u + k_v\delta v + k_{v'}\delta v' + k_w\delta w + k_{w'}\delta w' + k_\theta\delta\theta)\,dx\,dt + \mathbf{O}(\epsilon^4) \tag{A.9}$$

where

$$k_u = m_0\Omega^2 x + 2m_0\Omega\dot v - 2m_0\Omega\dot\theta(d_\eta\sin\bar\theta + d_\xi\cos\bar\theta)$$

$$-m_0\ddot u + m_0\ddot w'\left(d_\eta\sin\bar\theta + d_\xi\cos\bar\theta\right) + m_0\ddot v'\left(d_\eta\cos\bar\theta - d_\xi\sin\bar\theta\right)$$

$$+ m_0w'\ddot\theta\left(d_\eta\cos\bar\theta - d_\xi\sin\bar\theta\right) - m_0v'\ddot\theta\left(d_\eta\sin\bar\theta + d_\xi\cos\bar\theta\right) \tag{A.10}$$

$$k_v = -m_0\ddot v + m_0\Omega^2 v - 2m_0\Omega\dot u$$

$$+\left(m_0\Omega^2 + m_0\dot\theta^2 + 2m_0\Omega\dot v' + 2m_0\Omega w'\dot\theta\right)\left(d_\eta\cos\bar\theta - d_\xi\sin\bar\theta\right)$$

$$+\left(m_0\ddot\theta + 2m_0\Omega\dot w' - 2m_0\Omega v'\dot\theta\right)\left(d_\eta\sin\bar\theta + d_\xi\cos\bar\theta\right) \tag{A.11}$$

$$k_{v'} = -\left(2m_0\Omega\dot{v} + m_0\Omega^2 x\right)\left(d_\eta\cos\bar{\theta} - d_\xi\sin\bar{\theta}\right)$$

$$+ m_0\Omega\dot{\theta}\left(\left(k_{m\xi}^2 - k_{m\eta}^2\right)\sin 2\bar{\theta} + 2k_{m\eta\xi}^2\cos 2\bar{\theta}\right)$$

$$+ m_0\ddot{u}\left(d_\eta\cos\bar{\theta} - d_\xi\sin\bar{\theta}\right) \tag{A.12}$$

$$k_w = -m_0\ddot{w} - m_0\ddot{\theta}\left(d_\eta\cos\bar{\theta} - d_\xi\sin\bar{\theta}\right) + m_0\dot{\theta}^2\left(d_\eta\sin\bar{\theta} + d_\xi\cos\bar{\theta}\right) \tag{A.13}$$

$$k_{w'} = -\left(2m_0\Omega\dot{v} + m_0\Omega^2 x\right)\left(d_\eta\sin\bar{\theta} + d_\xi\cos\bar{\theta}\right)$$

$$+ 2m_0\Omega\dot{\theta}\left(k_{m\xi}^2\sin^2\bar{\theta} + k_{m\eta}^2\cos^2\bar{\theta} + k_{m\eta\xi}^2\sin 2\bar{\theta}\right)$$

$$+ m_0\ddot{u}\left(d_\eta\sin\bar{\theta} + d_\xi\cos\bar{\theta}\right) \tag{A.14}$$

$$k_\theta = -\left(2m_0\Omega\dot{v}w' + m_0\Omega^2 xw' + m_0\ddot{w}\right)\left(d_\eta\cos\bar{\theta} - d_\xi\sin\bar{\theta}\right)$$

$$+ \left(2m_0\Omega\dot{v}v' + m_0\Omega^2 xv' - m_0\Omega^2 v + m_0\ddot{v} + 2m_0\Omega\dot{u}\right)\left(d_\eta\sin\bar{\theta} + d_\xi\cos\bar{\theta}\right)$$

$$- 2m_0\Omega\dot{w}'\left(k_{m\xi}^2\sin^2\bar{\theta} + k_{m\eta}^2\cos^2\bar{\theta} + k_{m\eta\xi}^2\sin 2\bar{\theta}\right)$$

$$- m_0\Omega\dot{v}'\left[\left(k_{m\xi}^2 - k_{m\eta}^2\right)\sin 2\bar{\theta} + 2k_{m\eta\xi}^2\cos 2\bar{\theta}\right]$$

$$- \frac{1}{2}m_0\Omega^2\left[\left(k_{m\xi}^2 - k_{m\eta}^2\right)\sin 2\bar{\theta} + 2k_{m\xi\eta}^2\cos 2\bar{\theta}\right] - m_0 k_m^2\ddot{\theta}$$

$$- m_0\ddot{u}v'\left(d_\eta\sin\bar{\theta} + d_\xi\cos\bar{\theta}\right) + m_0\ddot{u}w'\left(d_\eta\cos\bar{\theta} - d_\xi\sin\bar{\theta}\right) \tag{A.15}$$

The terms with a single underline (bending–torsion) or double underline (extension-torsion, trapeze effect) do not appear in other studies developed for torsionally stiff rotor blades (Hodges and Dowell, 1974; Kaza and Kvaternik, 1977; Bir et al., 1990). The dash-underlined terms must be retained when the area centroids of the blade cross-sections are not coincident with the elastic axis (as in the case of circular arc airfoils). Note that the wave-underlined terms are one order of magnitude greater than the order of truncation. These terms are retained so that the elements of the mass matrix associated with the equation for the axial displacement u are non-zero. The cross-sectional constants are defined in Appendix C.

A.3. Tip mass kinetic energy

The variation in the kinetic energy of the tip mass is

$$(\delta T)_m = \{m_m\Omega^2 x_m + 2m_m\Omega\dot{v}_m - 2m_m T_1\Omega\dot{\theta}_m\}\delta u_m + \{m_m\Omega^2 v_m - m_m\ddot{v}_m - 2m_m\Omega\dot{u}_m + m_m T_1(\ddot{\theta}_m + 2\Omega\dot{w}_m - 2\Omega v_{,m}\dot{\theta}_m) + m_m$$

$$T_2(\Omega^2 + \dot{\theta}_m^2 + 2\Omega w_{,m}\dot{\theta}_m + 2\Omega\dot{v}_{,m})\}\delta v_m + \{2m_m T_5\Omega\dot{\theta}_m + m_m T_2(-2\Omega\dot{v}_m - \Omega^2 x_m)\}\delta v_m + \{-m_m\ddot{w}_m + m_m T_1\dot{\theta}_m^2 - m_m T_2\ddot{\theta}_m\}\delta w_m$$

$$+ \{2m_m T_3\Omega\dot{\theta}_m + m_m T_1(-2\Omega\dot{v}_m - \Omega^2 x_m)\}\delta w_m + \{m_m T_1(2\Omega\dot{v}_m v_m + \Omega^2 x_m v_m - \Omega^2 v_m^2 + \ddot{v}_m + 2\Omega\dot{u}_m)$$

$$+ m_m T_2(-2\Omega\dot{v}_m w_m - \Omega^2 x_m w_m - \ddot{w}_m) + m_m T_3(-\ddot{\theta}_m - 2\Omega\dot{w}_m) + m_m T_4(-\ddot{\theta}_m) + m_m T_5(-\Omega^2 - 2\Omega\dot{v}_m)\}\delta\theta_m + \boldsymbol{O}(\epsilon^4) \tag{A.16}$$

A.4. Tip mass gravitational energy

The variation in the gravitational potential energy of the tip mass is given by

$$(\delta V_g)_m = m_m g\delta z_m = m_m g\,\delta w_m - m_m g\,w_m\,T_1\,\delta w_m + m_m g\left(1 - \frac{w_m'^2}{2}\right)T_2\,\delta\theta_m \tag{A.17}$$

Appendix B. Aerodynamic constants

Assuming that the aerodynamic coefficients are of the following order,

$$\frac{C_{l0}}{C_{l\alpha}}, \frac{C_{m0}}{C_{l\alpha}} = \mathbf{O}(\epsilon) \tag{B.1}$$

$$\frac{C_{d0}}{C_{l\alpha}} = \mathbf{O}(\epsilon^2) \tag{B.2}$$

and introducing the dimensionless constants $\lambda_i = V_i/(\Omega R)$ and $r = x/R$, the generalized forces and moments associated with the aerodynamic loads are

$$a_v = -\frac{1}{2}\rho_\infty(\Omega x)^2 cC_{l\alpha}\left[\left(1+\frac{\dot{v}}{\Omega x}\right)\left(\frac{\lambda_i}{r}+\frac{\dot{w}}{\Omega x}\right)\sin\bar{\theta} - \left(\frac{\lambda_i}{r}+\frac{\dot{w}}{\Omega x}\right)^2\cos\bar{\theta}\right]C'$$

$$-\frac{1}{2}\rho_\infty(\Omega x)cC_{l\alpha}\left[\left(\frac{\lambda_i}{r}+\frac{\dot{w}}{\Omega x}\right)\left(\frac{c}{2}+x_A\right)\dot{\theta} + (\Omega vw' + \Omega xv'w')\sin\bar{\theta}\right]C'$$

$$-\frac{1}{2}\rho_\infty(\Omega x)^2 cC_{l0}\left(\frac{\lambda_i}{r}+\frac{\dot{w}}{\Omega x}\right)\cos\bar{\theta}\,C'$$

$$-\frac{c^2}{16}\rho_\infty(\Omega x)C_{l\alpha}\left[\left(\frac{\lambda_i}{r}+\frac{\dot{w}}{\Omega x}\right)(1-\cos 2\bar{\theta}) + \left(1+\frac{\dot{v}}{\Omega x}\right)\sin 2\bar{\theta}\right]\dot{\theta}$$

$$-\frac{c^2}{16}\rho_\infty C_{l\alpha}\left[\ddot{v}(1-\cos 2\bar{\theta}) - \ddot{w}\sin 2\bar{\theta} + \left(2x_A+\frac{c}{2}\right)\ddot{\theta}\sin\bar{\theta}\right]$$

$$-\frac{1}{2}\rho_\infty(\Omega x)^2\frac{c}{4}C_{d0}(3\cos\bar{\theta}+\cos 3\bar{\theta}) \tag{B.3}$$

$$a_w = -\frac{1}{2}\rho_\infty(\Omega x)^2 cC_{l\alpha}\left[\left(1+\frac{\dot{v}}{\Omega x}\right)\left(\frac{\lambda_i}{r}+\frac{\dot{w}}{\Omega x}\right)\cos\bar{\theta} - \left(1+\frac{\dot{v}}{\Omega x}\right)^2\sin\bar{\theta}\right.$$

$$\left.+\left(v'^2+\frac{w'^2}{2}\right)\sin\bar{\theta}\right]C'$$

$$+\frac{1}{2}\rho_\infty(\Omega x)cC_{l\alpha}\left[\left(\frac{c}{2}+x_A\right)\left(1+\frac{\dot{v}}{\Omega x}\right)\dot{\theta} + \Omega w'\left(\frac{c}{2}+x_A\right) - \Omega vw'\cos\bar{\theta}\right.$$

$$\left.+(2\Omega u + 2\Omega vv')\sin\bar{\theta}\right]C'$$

$$+\frac{1}{2}\rho_\infty(\Omega x)^2 cC_{l0}\left[\left(1+\frac{2\dot{v}}{\Omega x}\right)\cos\bar{\theta} + \left(\frac{\lambda_i}{r}+\frac{\dot{w}}{\Omega x}\right)\sin\bar{\theta}\right]C'$$

$$+\frac{c^2}{16}\rho_\infty(\Omega x)C_{l\alpha}\left[\left(1+\frac{\dot{v}}{\Omega x}\right)(1+\cos 2\bar{\theta}) + \left(\frac{\lambda_i}{r}+\frac{\dot{w}}{\Omega x}\right)\sin 2\bar{\theta}\right]\dot{\theta}$$

$$-\frac{c^2}{16}\rho_\infty C_{l\alpha}\left[\ddot{w}(1+\cos 2\bar{\theta}) - \ddot{v}\sin 2\bar{\theta} - \left(2x_A+\frac{c}{2}\right)\ddot{\theta}\cos\bar{\theta}\right]$$

$$-\frac{1}{2}\rho_\infty(\Omega x)^2\frac{c}{2}C_{d0}\sin\bar{\theta}(1+\cos 2\bar{\theta}) \tag{B.4}$$

$$a_\theta = \frac{1}{2}\rho_\infty(\Omega x)^2\frac{c^2}{2}C_{m0}(1+\cos 2\bar{\theta})C'$$

$$+\frac{1}{2}\rho_\infty(\Omega x)^2\frac{c}{2}x_A C_{l\alpha}\left[2\left(\frac{\lambda_i}{r}+\frac{\dot{w}}{\Omega x}\right)\cos 2\bar{\theta} - \left(1+\frac{2\dot{v}}{\Omega x}\right)\sin 2\bar{\theta}\right]C'$$

$$-\frac{1}{2}\rho_\infty(\Omega x)cx_A C_{l\alpha}\left[\left(\frac{c}{2}+x_A\right)\dot{\theta}\cos\bar{\theta}\right]C'$$

$$-\frac{c^2}{16}\rho_\infty(\Omega x)C_{l\alpha}(c+2x_A)\dot{\theta}\cos\bar{\theta}$$

$$-\frac{1}{2}\rho_\infty(\Omega x)^2\frac{c}{2}x_A C_{l0}(1+\cos 2\bar{\theta})C' \tag{B.5}$$

The terms with a solid underline are significant for large pitch angles and the terms with a dashed underline disappear for symmetric airfoil sections.

Appendix C. Cross-sectional constants

The cross-sectional constants used to calculate the strain energy are given by

$$
\begin{aligned}
&\iint_A d\eta d\xi = A \qquad \iint_A \eta^2\, d\eta d\xi = I_\xi \qquad\qquad \iint_A (\eta^2+\xi^2)^2\, d\eta d\xi = B_1\\
&\iint_A \eta\, d\eta d\xi = Ae_\eta \quad \iint_A \xi^2\, d\eta d\xi = I_\eta \qquad\quad \iint_A \eta(\eta^2+\xi^2)\, d\eta d\xi = B_2\\
&\iint_A \xi\, d\eta d\xi = Ae_\xi \quad \iint_A \eta\xi\, d\eta d\xi = I_{\eta\xi} \qquad \iint_A \xi(\eta^2+\xi^2)\, d\eta d\xi = B_3\\
&\qquad\qquad\qquad \iint_A (\eta^2+\xi^2)\, d\eta d\xi = J = Ak_A^2
\end{aligned}
$$

It can be seen that e_η and e_ξ are the coordinates of the tensile axis (loci of the area centroids) relative to the elastic axis, positive in the direction of the η- and ξ- axes respectively.

The cross-sectional constants used to calculate the blade kinetic energy are given by

$$
\begin{aligned}
&\int_A \rho\, d\eta d\xi = m_0 \qquad \int_A \rho\, \eta^2\, d\eta d\xi = m_0 k_{m_\xi}^2 \quad \int_A \rho(\eta^2+\xi^2)\, d\eta d\xi = m_0 k_m^2\\
&\int_A \rho\, \eta\, d\eta d\xi = m_0 d_\eta \quad \int_A \rho\, \xi^2\, d\eta d\xi = m_0 k_{m_\eta}^2\\
&\int_A \rho\, \xi\, d\eta d\xi = m_0 d_\xi \quad \int_A \rho\, \eta\xi\, d\eta d\xi = m_0 k_{m_{\eta\xi}}^2
\end{aligned}
$$

where m_0 represents the mass per unit length of the rotor blade, d_η and d_ξ are the mass centroid offsets from the elastic axis, respectively in the η and ξ directions, and $m_0 k_{m_\xi}^2$ and $m_0 k_{m_\eta}^2$ are the chordwise and flatwise mass moment of inertia of the blade section about the elastic axis.

The constants used to calculate the tip mass kinetic energy are

$$
m_m = \int_{-L_1}^{L_2} \iint_{A_m} \rho_m\, dA_m\, d\lambda \tag{C.1}
$$

$$
m_m T_1 = \int_{-L_1}^{L_2} \iint_{A_m} \rho_m(\eta \sin + \xi \cos)\, dA_m\, d\lambda = m_m\left[\eta_m \sin\overline{\theta}_m + \xi_m \cos\overline{\theta}_m + \frac{L_2-L_1}{2}\sin(\overline{\theta}_m-\theta_{ind}) \right] \tag{C.2}
$$

$$
m_m T_2 = \int_{-L_1}^{L_2} \iint_{A_m} \rho_m(\eta \cos - \xi \sin)\, dA_m\, d\lambda = m_m\left[\eta_m \cos\overline{\theta}_m - \xi_m \sin\overline{\theta}_m + \frac{L_2-L_1}{2}\cos(\overline{\theta}_m-\theta_{ind}) \right] \tag{C.3}
$$

$$
\begin{aligned}
m_m T_3 = \int_{-L_1}^{L_2} \iint_{A_m} \rho_m(\eta \sin + \xi \cos)^2\, dA_m\, d\lambda &= m_m\left[\eta_m^2 \sin^2\overline{\theta}_m + \xi_m^2 \cos^2\overline{\theta}_m + \eta_m\xi_m \sin 2\overline{\theta}_m \right.\\
&\left. + \frac{L_2-L_1}{2}(2\eta_m \sin\overline{\theta}_m \sin(\overline{\theta}_m-\theta_{ind}) + 2\xi_m \cos\overline{\theta}_m \sin(\overline{\theta}_m-\theta_{ind})) + \frac{L_1^3+L_2^3}{3(L_1+L_2)}\sin^2(\overline{\theta}_m-\theta_{ind}) \right]
\end{aligned} \tag{C.4}
$$

$$
\begin{aligned}
m_m T_4 = \int_{-L_1}^{L_2} \iint_{A_m} \rho_m(\eta \cos - \xi \sin)^2\, dA_m\, d\lambda &= m_m\left[\eta_m^2 \cos^2\overline{\theta}_m + \xi_m^2 \sin^2\overline{\theta}_m - \eta_m\xi_m \sin 2\overline{\theta}_m \right.\\
&\left. + \frac{L_2-L_1}{2}(2\eta_m \cos\overline{\theta}_m \cos(\overline{\theta}_m-\theta_{ind}) - 2\xi_m \sin\overline{\theta}_m \cos(\overline{\theta}_m-\theta_{ind})) + \frac{L_1^3+L_2^3}{3(L_1+L_2)}\cos^2(\overline{\theta}_m-\theta_{ind}) \right]
\end{aligned} \tag{C.5}
$$

$$
\begin{aligned}
m_m T_5 = \int_{-L_1}^{L_2} \iint_{A_m} \rho_m(\eta \sin + \xi \cos)(\eta \cos - \xi \sin)\, dA_m\, d\lambda &= m_m\left[(\eta_m^2-\xi_m^2)\sin\overline{\theta}_m \cos\overline{\theta}_m + \eta_m\xi_m \cos 2\overline{\theta}_m \right.\\
&\left. + \frac{L_2-L_1}{2}(\eta_m \sin(2\overline{\theta}_m-\theta_{ind}) + \xi_m \cos(2\overline{\theta}_m-\theta_{ind})) + \frac{L_1^3+L_2^3}{3(L_1+L_2)}\sin(\overline{\theta}_m-\theta_{ind})\cos(\overline{\theta}_m-\theta_{ind}) \right]
\end{aligned} \tag{C.6}
$$

References

Bir, G., Chopra, I., Nguyen, K., 1990. Development of UMARC (University of Maryland Advanced Rotorcraft Code). In: Proceedings of American Helicopter Society 46th Annual Forum. Washington, D.C., 21–23 May.

Goldman, R.L., 1960. Some observations on the dynamic behavior of extremely flexible rotor blades. In: Paper 60-44, Proceedings of the 28th Annual Meeting of the Institute of the Aeronautical Sciences. New York, 25–27 January.

Hassig, H.J., 1971. An approximate true damping solution of the flutter equation by determinant iteration. J. Aircr. 8, 885–889. http://dx.doi.org/10.2514/3.44311.

Hodges, D.H., 2006. Nonlinear composite beam theory.. In: Lu, Frank K. (Ed.), Progress in Astronautics and Aeronautics 213. American Institute of Aeronautics and

Astronautics, Inc.,, Reston, VA.

Hodges, D.H., Pierce, G.A., 2002. Introduction to Structural Dynamics and Aeroelasticity. Cambridge University Press, New York, NY.

Hodges, D.H., 1985. Nonlinear Dynamic Analysis of Pretwisted Beams Undergoing Small Strain and Large Rotations. Technical Paper NASA TP 2470. National Aeronautics and Space Administration.

Hodges, D.H., Dowell, E.H., 1974. Nonlinear Equations of Motion for the Elastic Bending and Torsion of Twisted Nonuniform Rotor Blades. Technical Note NASA TN D-7818. Ames Research Center and U.S. Army Air Mobility R & D Laboratory. Moffett Field, CA.

Johnson, W., 2013. Rotorcraft Aeromechanics. Cambridge University Press, New York, NY.

Kaza, K.R.V., Kvaternik, R.G., 1977. Nonlinear Aeroelastic Equations for Combined Flapwise Bending, Chordwise Bending, Torsion and Extension of Twisted Nonuniform Rotor Blades in Forward Flight. Technical Memorandum NASA TM 74059. Langley Research Center, National Aeronautics and Space Administration. Hampton, VA.

Linden, A.W., 1972. Variable Diameter Rotor Study. Technical Report TR 71 170. Air Force Flight Dynamics Laboratory. Dayton, OH.

Roeseler, W.G., 1966. The Effect of Ribbon Rotor Geometry on Blade Response and Stability (Master's thesis). Massachusetts Institute of Technology, Cambridge, MA.

Rosen, A., Friedmann, P.P., 1978. Nonlinear equations of equilibrium for elastic helicopter or wind turbine blades undergoing moderate deformation. Contractor Report NASA CR 159478. Lewis Research Center, National Aeronautics and Space Administration. Cleveland, OH.

Sicard, J., Sirohi, J., 2012. Experimental study of an extremely flexible rotor for microhelicopters. J. Aircr. 49, 1306–1314. http://dx.doi.org/10.2514/1.C031643.

Sicard, J., Sirohi, J., 2013. Measurement of the deformation of an extremely flexible rotor using digital image correlation. Meas. Sci. Technol. 24, 065203. http://dx.doi.org/10.1088/0957-0233/24/6/065203.

Sicard, J., Sirohi, J., 2014a. An analytical investigation of the trapeze effect acting on a thin flexible ribbon. J. Appl. Mech. 81.

Sicard, J., Sirohi, J., 2014b. Modeling of the large torsional deformation of an extremely flexible rotor in hover. AIAA J. 52, 1604–1615. http://dx.doi.org/10.2514/1.J052617.

Winston, M.M., 1968a. A Hovering Investigation of An Extremely Flexible Lifting Rotor. Technical Note NASA TN D-4820. Langley Research Center, National Aeronautics and Space Administration. Langley Station, VA.

Winston, M.M., 1968b. An Investigation of Extremely Flexible Lifting Rotors. Technical Note NASA TN D-4465. Langley Research Center, National Aeronautics and Space Administration. Langley Station, VA.